Techniques for the measurement of disruption halo currents in the National Spherical Torus Experiment

S. P. Gerhardt,[1] E. Fredrickson,[1] L. Guttadora,[1] R. Kaita,[1] H. Kugel,[1] J. Menard,[1] and H. Takahashi[2]
[1]*Princeton Plasma Physics Laboratory, Plainsboro, New Jersey 08540, USA*
[2]*Princeton Fusion Research LLC, Princeton, New Jersey 08540, USA*

This paper describes techniques for measuring halo currents, and their associated toroidal peaking, in the National Spherical Torus Experiments [M. Ono *et al.*, Nucl. Fusion **40**, 557 (2000)]. The measurements are based on three techniques: (1) measurement of the toroidal field created by the poloidal halo current, either with segmented Rogowski coils or discrete toroidal field sensors, (2) the direct measurement of halo currents into specially instrument tiles, and (3) small Rogowski coils placed on the mechanical supports of in-vessel components. For the segmented Rogowski coils and discrete toroidal field detectors, it is shown that the toroidal peaking factor inferred from the data is significantly less than the peaking factor of the underlying halo current distribution, and a simple model is developed to relate the two. For the array of discrete toroidal field detectors and small Rogowski sensors, the compensation steps that are used to isolate the halo current signal are described. The electrical and mechanical design of compact under-tile resistive shunts and mini-Rogowski coils is described. Example data from the various systems are shown. © *2011 American Institute of Physics*. [doi:10.1063/1.3642618]

I. INTRODUCTION

Tokamak[1] discharges are often terminated by events known as disruptions, where instabilities cause the plasma thermal energy to be lost in ∼1 ms, followed by a rapid decay of the plasma current.[2–5] Control of the plasma vertical position is often lost during these events, with the plasma moving up (or down) and impacting the top (or bottom) of the device; this plasma motion is known as a vertical displacement event (VDE).[2,3] When this happens, currents can flow from the plasma to in-vessel components, and then back to the plasma. These currents are, for the purpose of this paper, called halo currents. The poloidal component of those vessel/structure currents, when crossed with the tokamak toroidal field, can lead to potentially damaging forces on those components. Furthermore, if the currents are toroidally localized, the local force will be much larger than that inferred from measurements of the toroidally averaged current. Hence, it is important to understand how the peaking of those currents is related to the toroidally average halo current, and how those values are related to the total plasma current and other plasma parameters. For instance, understanding the distribution, magnitude, and temporal evolution of halo currents is a critical for the design of large tokamak experiments such as ITER.[6,7]

The purpose of this paper is to describe instrumentation for the measurement of these halo currents in the National Spherical Torus Experiment (NSTX).[8] NSTX is a medium-sized spherical tokamak,[9] designed to test the possible stability and transport advantages that can come from the low-aspect ratio geometry, compared to more traditional tokamaks.[1] The major radius is $R_0 = 0.85$ m and aspect ratios are typically in the range of $R_0/a = 1.3$–1.55 (a is the minor radius, defined as half the distance between the inboard and outboard plasma boundaries at the midplane). The toroidal field strength at the magnetic axis is typically in the range 0.35–0.55 T, while the plasma current is typically in the range 0.6–1.3 MA. Plasmas are typically heated up to 7.5 MW of neutral beams and/or up to 6 MW of 30-MHz high-harmonic fast waves. The vacuum vessel is composed of "inner" and "outer" vacuum vessels, corresponding to small and large major radius; this allows coaxial helicity injection studies of plasma start-up. The insulating breaks between the two vessels are located in the divertor region at the top and the bottom of the device. The two vessel sections are connected by a copper buswork under the device.

The instrumentation utilized for halo current detection in NSTX is shown schematically in Fig. 1 and are indicated in the photograph in Fig. 2. There are Rogowski sensors [10] wrapped around the center column, both at the top and bottom of the machine, to measure currents flowing on the center column. The CSCL1 Rogowski sensor has been split into three segments. Two arrays of discrete toroidal field sensors, known as the "inner ring" and "outer ring," are mounted to the vacuum chamber floor, and measure the current flowing in the chamber wall. Discrete "instrumented" tiles are located at six toroidal angles in each of two rows of tiles, and measure the current flowing into or out of the tiles.

A unique feature of NSTX is the liquid lithium divertor (LLD), installed inside NSTX in the fall of 2009. This structure, visible as four gray trays in Fig. 2, is composed of four 2.22-cm-thick copper plates. Each tray has a 0.025 cm thick stainless steel liner brazed to its surface, with a 0.01 cm thick layer of porous molybdenum flame sprayed on top. Each tray has a single point electrical connection to the divertor floor, with insulating supports at the tray corners. There are small Rogowski sensors on each of these "center post grounds," in order to measure disruption currents into the trays. More
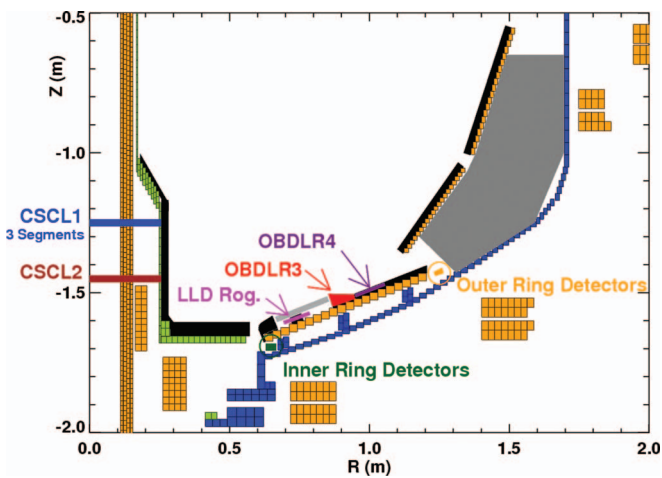
FIG. 1. (Color online) Layout of halo current diagnostics in NSTX. Not shown are the center-stack casing Rogowski coils (CSCU1 and CSCU2) located on the upper center column, in an orientation identical to the CSCL1 and CSCL2 sensors. The inner and outer ring detectors are circled.

physics motivation and engineering details regarding the liquid lithium divertor can be found in Ref. 11.

Note that halo currents have been measured in many tokamaks in the past. Discrete toroidal field sensors similar to those used in NSTX were utilized in JET[12–14] and Compass-D.[15] Segmented Rogowski coils have been utilized in Alcator C-Mod[16] and MAST.[17,18] Resistive shunts placed under tiles were utilized to measure halo currents in DIII-D[19,20] and ASDEX-Upgrade.[21,22] Additionally, small Rogowski coils linking in vessel structural supports have been used in MAST,[17,18] JET,[13,14] and JT-60,[23] and small Rogowski sensors mounted under single-point-grounded tiles have been proposed[24] and implemented[25] for JET.

The outline of this paper is as follows. Section II shows that for segmented Rogowskis on the center-column of the device, modeling is required to relate the measured and actual toroidal peaking factors. The details and limitations of such a model are described. This problem remains, but is less significant, for the array composed of discrete toroidal field sensors mounted to the vessel floor, described in Sec. III. A challenging analysis task with these sensors is to correctly isolate the halo-current signal from pickup due to the coils, plasma current, and induced vacuum vessel currents. Section IV describes compact instrumentation for measuring the current into individual tiles in the lower divertor. The mechanical and electrical design for the compact resistive-shunt-based detectors is presented, and example data are shown. Section V describes the Rogowski sensors used to measure halo currents flowing into LLD and shows example data. The physics results from these instruments will be presented in subsequent publications.

II. INTERPRETATION OF MEASUREMENTS FROM THE CENTER COLUMN SEGMENTED ROGOWSKI COILS

For the spherical torus configuration, where the toroidal field is much stronger on the inboard side than the outboard ($B_T \propto 1/R$), poloidal halo currents on the center-column are a great threat to the integrity of the device.[26] In order to assess these currents, Rogowski coils were placed around the inconel tube ("Center Stack Casing," or "CSC") that provides the inboard vacuum boundary. The carbon tiles on the center column had special slots machined on their backsides to allow room for the Rogowski coils. As shown by the bands in Figs. 1 and 2, these Rogowski coils are oriented in the horizontal plane so as to detect the toroidal field created by
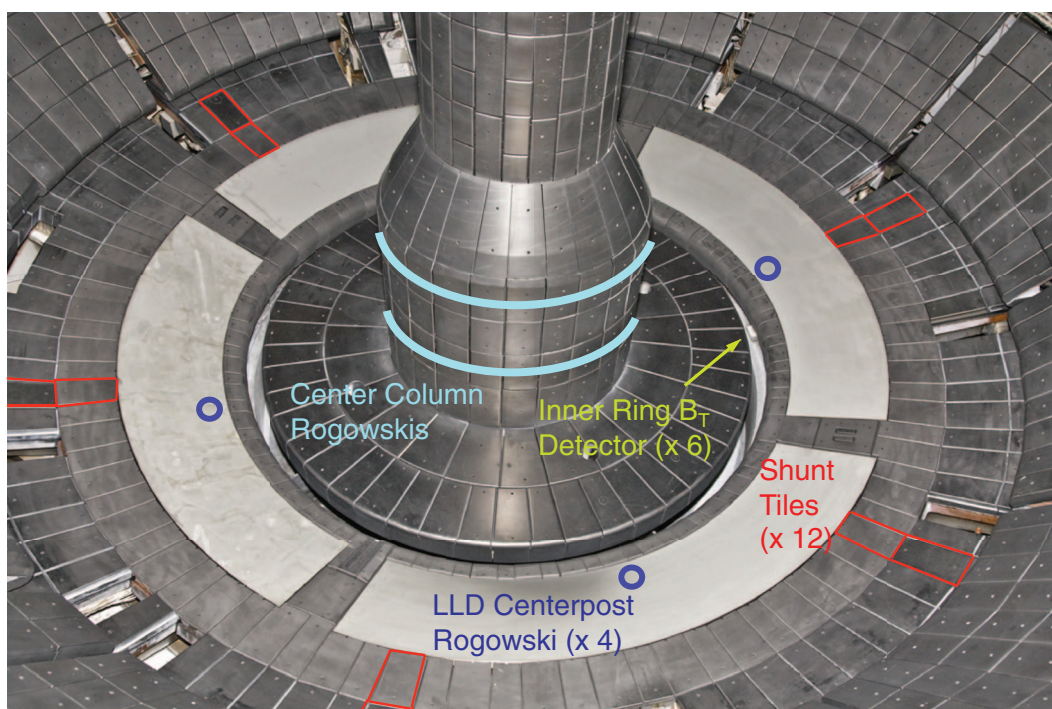

FIG. 2. (Color online) Photograph of the NSTX lower divertor, with the locations of halo current instrumentation called out. Indicated in the figure are the shunt tiles, LLD Rogowski coils, a single "inner ring" detector, and the locations of the center-stack casing Rogowski coils.

currents flowing vertically in the center stack casing. Measurement of the total CSC halo current using these instruments is straightforward using the standard Rogowski formulas.[10]

The upper Rogowski coil in the lower divertor (CSCL1) is divided into three sections to assess the toroidal peaking of the halo current. The measured toroidal peaking factor is given by

$$(TPF)_{B_T} = \frac{N \cdot \max(B_{T,HC,i}, i = 1:N)}{\sum_i B_{T,HC,i}}, \tag{1}$$

where N is the number of segments in the Rogowski sensor and $B_{T,HC,i}$ is the average toroidal field measured by the ith segment of the Rogowski coil. However, this measure of the peaking factor can severely underestimate the actual halo current, defined as

$$(TPF)_{HC} = \frac{\max(J_{HC})}{mean(J_{HC})}. \tag{2}$$

Here, J_{HC} is the poloidal current density in the component of interest.

This underestimation can be understood by considering the limiting case of a single filament of halo current flowing up the CSC at a single toroidal angle. The actual toroidal peaking factor, defined as the maximum halo current normalized by the average halo current, would approach infinity. However, finite signal would be detected on all the Rogowski coil segments, and the inferred toroidal peaking factor would be much less than the actual value. Said another way, the toroidal field distribution due to poloidal currents on the center column is less toroidally peaked than the underlying current distribution. The segmented Rogowski measures the toroidal field distribution, and will necessarily underestimate the actual current peaking.

Based on these arguments, a relationship must be defined between the measured and actual toroidal peaking factors. This relationship can be deduced from cylindrical *model* of the system as follows. A toroidal distribution of vertically flowing current on the 0.25-m radius center-stack casing is assumed. In the present modeling, the following distribution is used:

$$I_{HC}(\phi) = 1 + A_{HC} \cos(\phi - \phi_{HC}). \tag{3}$$

This provides a simple approximation to the toroidal structure observed in various devices, where $n = 1$ (as well as potentially higher n) structures are observed. The toroidal peaking factor (*TPF*) of this distribution is then $(TPF)_{HC} = 1 + A_{HC}$. The average toroidal field along each of the N Rogowski segments is then computed, and the peaking factor of the toroidal field is computed as in Eq. (1).

An additional source of uncertainty comes from the relative phase of the halo current distribution with respect to the fixed Rogowski segments.[14] Imagine again a hypothetical single filament of vertical current at one toroidal angle and a segmented Rogowski coil with two segments. If a break between the two segments falls at the toroidal angle of the filament, then the two segments will measure the same signal, and the inferred toroidal peaking will be 1. On the other hand, if one
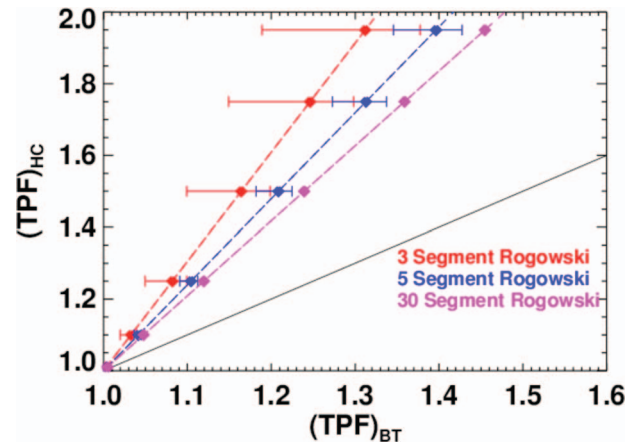

FIG. 3. (Color online) The TPF of the halo current distribution, compared to that inferred from segmented Rogowski sensors, which sample the toroidal field. Results are from a cylindrical model of segmented Rogowski sensors and halo currents on the center column, with an $n = 1$ cosine toroidal variation. The dashed lines are fits as per Eq. (4).

of the segments is centered on the filament, then the toroidal peaking factor will be >1 (though still much smaller than the actual peaking factor). In order to account for this variation, the calculation described in the previous paragraph is then repeated for many value of the parameter ϕ_{HC}, but with fixed segment locations; the range of "measured" peaking factors $(TPF)_{BT}$ is then used provide an uncertainty estimate.

The results of these simulations are shown in Fig. 3, for Rogowski coils with 3, 5, and 30 segments. For a three-segment Rogowski sensor like in NSTX, a true toroidal peaking factor of 2 leads to a measured peaking factor of ∼1.3. The measured peaking factor increases as the number of Rogowski coil segments is increased; however, the effect saturates as the number of segments is increased beyond ∼8. Increasing the number of segments does, however, reduce the uncertainty due to the relative phases of the halo current and the Rogowski sensors, since the shorter Rogowski segments are able to more accurately sample the local toroidal field.

With this modeling, we can relate the measured and halo current peaking factors as follows:

$$(TPF)_{HC} = A_0 + A_1 (TPF)_{BT}. \tag{4}$$

The values of A_0 and A_1 are given in Table I for various numbers of segments. Also given are the same coefficients, calculated from the same model with the more toroidally peaked Gaussian current distribution

$$I_{HC}(\theta) = 1 + A_{HC} e^{\left(-\frac{(\theta - \theta_{HC})^2}{0.5^2}\right)}, \tag{5}$$

where the angle θ is in radians. Compared to the form in Eq. (3), the form in Eq. (5) has the advantage that by changing the parameter A_{HC}, the toroidal peaking factor can be increased above 2. With the coefficients in this table, it is possible to correct the measurements to estimate the actual peaking of currents in the center column, after making an *assumption* about the underlying toroidal distribution.

TABLE I. Coefficients relating the quantities $(TPF)_{BT}$ and $(TPF)_{HC}$ via Eq. (4), for the six-sensor arrays. The inner ring coefficients are based on the green current path in Fig. 4, while the outer ring coefficients are based on the orange path.

Sensor	Current distribution	A_0	A_1
Inner	Cosine	−0.30	1.30
Inner	Gaussian	−1.06	2.06
Outer	Cosine	−0.21	1.21
Outer	Gaussian	−0.869	1.87

III. POLOIDAL HALO CURRENTS MEASUREMENTS BASED ON DISCRETE TOROIDAL FIELD SENSORS

A. TPF underestimation

A separate set of sensors has been installed to measure poloidal currents in the vessel wall of NSTX at two poloidal locations, denoted as the "Inner Ring" and "Outer Ring" in Fig. 1. Each poloidal location has a set of six discrete toroidal field sensors, which are approximately equally spaced in toroidal angle. The sensors are mounted inside the vacuum chamber, approximately 0.5 cm off the vacuum chamber wall. These sensors detect the toroidal field due to poloidal currents in the nearby vessel walls and components. They can be viewed as a segmented Rogowski coil, in the limit that each segment is of negligible toroidal extent. It is thus important to model the performance of these sensors, in order to determine to what extent they also may underestimate the toroidal peaking of the halo current.

The simple model we have constructed for this test assumes that the halo current flow in the poloidal plane (i.e., the toroidal component of the halo current in neglected), but with
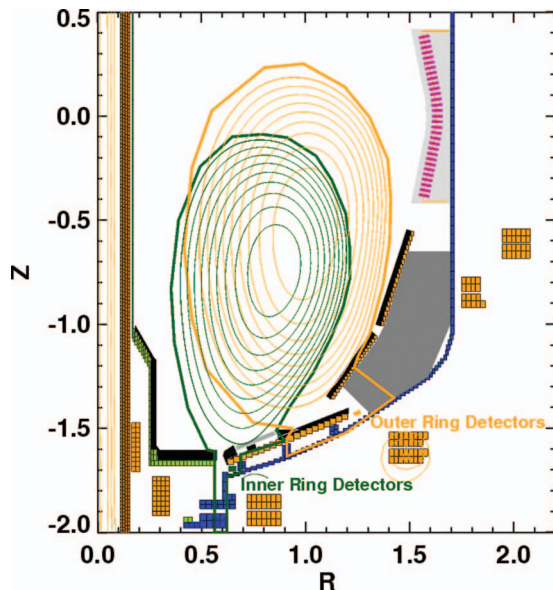

FIG. 4. (Color online) Poloidal halo current path used in the performance modeling for the discrete B_T sensors. The thick solid lines are the modeled halo current paths, while the thin lines are the poloidal flux contours of plasma immediately preceding a disruption. The sensors themselves are indicated in the figure, with the same color as the halo current path that links them.
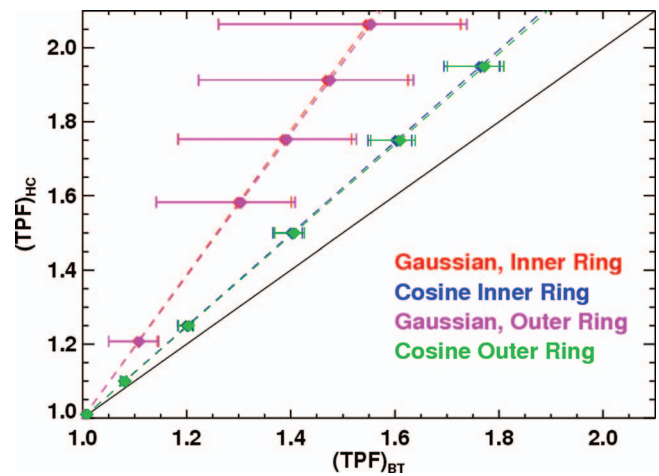

FIG. 5. (Color online) $(TPF)_{HC}$ vs. $(TPF)_{BT}$, for the discrete B_T sensors on the lower vessel wall. The halo current paths utilized for the two sensor arrays are illustrated in Fig. 4. Both the cosine [see Eq. (3)] and Gaussian [see Eq. (5)] toroidal distributions are utilized in the calculations.

a toroidal distribution given by either Eq. (3) or Eq. (5). In one model current path (see Fig. 4), current enters the lower divertor floor, flows along the divertor plate, down the bus work that connects the inner and outer vessels, out of the inner divertor, and around over the plasma top, thus completing the circuit. This path would produce net current detected in the inner ring of B_T detectors, but not in the outer ring. In the second model current path, also illustrated in Fig. 4, the current flows into the secondary passive plate, through the vessel wall, and out of the divertor floor to the plasma. This path will produce net current in the outer ring of B_T detectors, but not in the inner ring.

The results of such calculations are shown in Fig. 5. For the Gaussian distribution, there is once again an underestimation of the current toroidal peaking (see Table II for the fit coefficients as in Eq. (4)), though not as great as for the segmented Rogowski coils. The uncertainty associated with the toroidal phase of the current perturbation compared to the detector phase is fairly small, as the six sensors sample the $n = 1$ field reasonably well. The more toroidally peaked Gaussian distribution, however, shows considerable variation in the measured TPF for a given current distribution; there are large differences in the measured TPFs if the peak in the current falls at the toroidal angle of the sensors, or between two sensors.

TABLE II. Coefficients relating the quantities $(TPF)_{BT}$ and $(TPF)_{HC}$ via Eq. (4).

No. of segments	Current distribution	A_0	A_1
3	Cosine	−2.04	3.04
5	Cosine	−1.40	2.40
30	Cosine	−1.10	2.10
3	Gaussian	−7.03	8.03
6	Gaussian	−2.85	3.85
30	Gaussian	−1.53	2.53

B. Resolving the signal due to the disruption halo current

When the array of detectors is considered as a segmented Rogowski, it becomes clear that they will measure the TF rod current (i.e., the net current flowing down the center columns, which produces the toroidal magnetic field). It might at first appear that this contribution would overwhelm the signal from the halo currents. However, spherical tokamaks typically operate with ratios of rod current to plasma current less than 2; typical values of rod and plasma currents in NSTX are 1.7–2.1 MA and 0.8–1.2 MA. Halo current fractions, on the other hand, can be 10%–30% of the plasma current. Hence, the halo current signal can be a reasonable fraction (5%–20%) of the signal from the TF, and can be easily extracted. There is no need to AC couple the sensors in this case, which makes calibration checks quite simple using vacuum toroidal field shots to provide a known field at the sensor.

In addition to the direct pickup of the torodial field coil current, other sources of signal unrelated to halo currents have also been observed. This additional pickup is due to the finite effective area in the poloidal direction due to sensor misalignments and winding imperfections. Sources of poloidal field include: (1) the direct pickup of the poloidal field from the PF coils, (2) direct pickup of the poloidal field from the plasma current, and (3) pickup of field from induced toroidal currents flowing in the vacuum vessel wall.

The method of processing the sensor data to isolate the halo current signal proceeds as follows. First, the "raw" integrated signal in volts is multiplied by a calibration coefficient to convert the field to tesla. The static coil pickup is then subtracted from the signal, using a weighted sum of coil currents; both the toroidal field coils and all the poloidal field coils are included in this step. The weight factors are determined from single-coil vacuum shots. This process will be referred to as "static compensation" below, and the results of this step are shown in Fig. 6(a).

The other two sources of pickup noted above are harder to compensate. The pickup of the poloidal field from the plasma will depend strongly on the plasma vertical position, X-point location, and internal profiles. All three of these quantities change rapidly during a disruption, and therefore, a simple subtraction as with the coil pickup is not possible. Similarly, the induced toroidal eddy currents during the disruption are quite large. NSTX routinely uses the voltage on flux loops mounted on the chamber wall to measure these currents;[27] however, we have found that correcting the halo current sensor data with these vessel current measurements introduced additional undesirable temporal variations. Finally, note that there are no dedicated poloidal field sensors in the immediate vicinity of the B_T sensors; this precludes using actual B_P measurements to calculate local poloidal field for additional correction of the sensor data.

Given these issues, we have developed a moving-baseline technique for isolating the halo current signal. The static compensated data are median filtered with a window of typically 14–18 ms; this is shown in Fig. 6(a). This window is wider than the majority of halo currents pulses, but shorter than the typical evolution of the plasma motion and coil current vari-
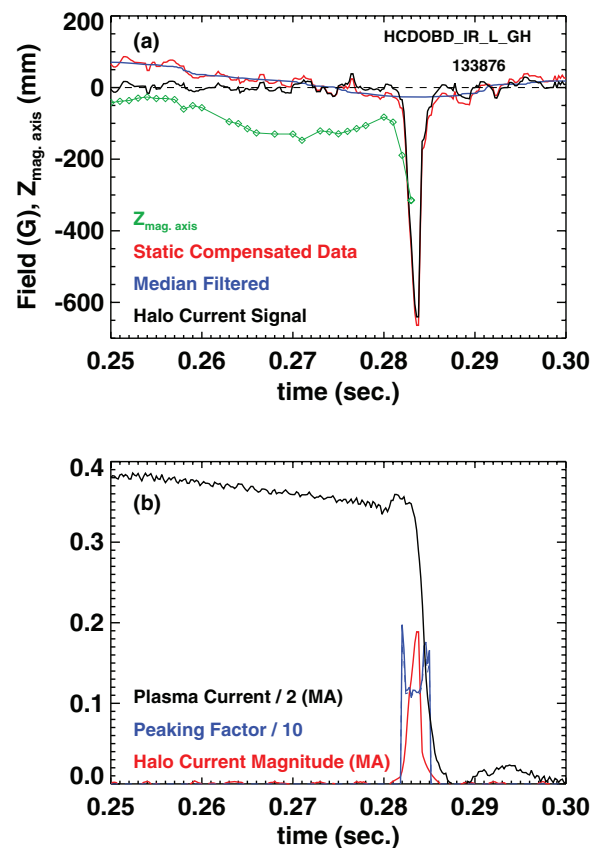

FIG. 6. (Color online) (a) Moving baseline subtraction methods used to determine the signal due to the poloidal halo current as well as the magnetic axis vertical position, and (b) halo current and plasma current waveforms for this discharge. Note the scaling on the plasma current and peaking factor in this second figure.

ation. The median-filtered signal is then subtracted from the compensated data, thereby leaving behind only the rapid spike associated with the halo current (black in the figure). Once this process has been applied to all the six signals, the total current linking the sensor ring, and thus, flowing in the chamber wall (shown in Fig. 6(b)) is given by.

$$I_{linked} = \frac{2\pi R_s}{6\mu_0} \sum_{i=1}^{6} B_{T,i},$$

where R_s is the radius of the sensors. The toroidal peaking factor (of the measured field) is calculated as per Eq. (1), and can be corrected using the coefficients in Table II.

The result from a typical halo current analysis is shown in Fig. 6(b), where the total halo current measured by the inner ring detectors is shown as a function of time, along with the toroidal peaking factor, corrected as per Eq. (4), and the plasma current.

IV. DIRECT HALO-CURRENT MEASUREMENTS VIA INSTRUMENTED TILES

The techniques described in the previous section are useful for measuring the current flowing in the metal vacuum boundaries in NSTX (the center-stack casing and vessel bottom). They do not, however, easily resolve the locations where
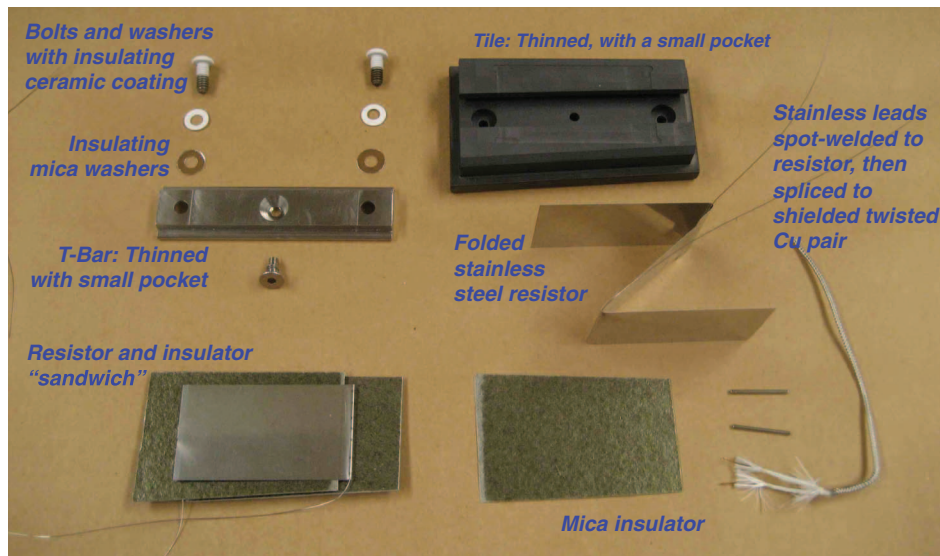
FIG. 7. (Color online) Components of the instrumented tile design. See text for further details.

currents enter and exit the in-vessel components. In order to locate these exit and entry points, a number of graphite divertor tiles have been instrumented to measure the current flowing into or out of them. Essentially, a shunt resistor of known resistance is placed under each tile. The voltage on the resistor is brought out of the vessel on two leads, is digitized, and then used to infer the current flowing into the tile.

This system was first implemented for the 2009 run campaign, with four tiles located in row 3 of lower outboard divert tiles, and spaced from each other by 90° in the toroidal direction. The radius of these tiles (R = 0.9 m) is outside that of the lower outer strike-point for the vast majority of NSTX discharges. This system of sensors was expanded for the 2010–2012 run campaigns, with six sensors in the row 3 tiles of the outer divertor, and six sensors in the row 4 tiles; this arrangement is indicated as the red outlines in Fig. 2, where the row 3 tiles are those at smaller major radius.

The components of the instrumented tile sensor are shown in Fig. 7. The key component of the sensor is the resistive shunt element, fabricated from 0.025-cm-thick stainless steel shim-stock. A strip of this material is folded into a "Z" shape. Two 0.051-cm-thick mica insulators are inserted into the "Z"s to insulate the separate folds. One side of the Z is fit inside a 0.02-cm deep pocket machined on the back of the tile. When the tile is then installed in NSTX, one side of the "Z" presses against the tile, while the other presses against the divertor floor, and hence, the vacuum chamber, through a grafoil sheet.

A 0.038 cm stainless steel wire is spot-welded to the inside of each bend in the stainless "Z." The diameter of the stainless wires was chosen to be smaller than the mica sheets, so that the total thickness of the compressed "Z" is given by three stainless steel layers and two mica sheets. Stainless steel wire was chosen because of the ease of welding this material to the stainless steel shunt. Given that these wires only transmit the shunt voltage and carry essentially no current, the increased resistivity of the stainless steel compared to copper is not important.

This design relies on the resistor being the only path to ground for currents entering the tile; multiple steps are taken in order to ensure that this is the case. The tile is fastened to the grounded divertor plate via a bolted T-bar. The T-bar itself is in electrical contact with the tile. However, the washers and upper-half of the bolts are given a ceramic coating, which isolates them from the T-bar and tile. Additional isolation is ensured by the insertion of mica washers under the ceramic-coated washers. It is also critical that the tile does not touch any adjacent tiles; during the installation, some sections of the tile were grounded off to ensure gaps of 0.25 cm on all sides. Finally, the thickness and width of the shunt element were chosen such that the voltage on the shunt during the largest expected halo current is <5 V. This low voltage helps to prevent arcs to adjacent tiles.

The stainless steel signal leads have a length of approximately 2 ft. They are then spliced using hypodermic needle to stainless steel jacketed copper twisted pair. The copper twisted pair is then brought to the vacuum electrical feedthrough, and then via shielded twisted pair to isolation amplifiers. Isolation amplifiers with 100 kHz bandwidth [Analog Devices AD-215] are used to isolate the signals from the data acquisition system (recall that one of the leads is directly connected to the NSTX vacuum vessel, and thus, cannot be connected directly to the data acquisition system).

While the resistance of the shunt can be easily calculated from the known dimensions and resistance of the stainless steel, we have found that *in situ* calibration of the system is quite useful. A low-voltage power supply with maximum current of ∼20 A is used, with one lead connected to the NSTX vessel, and the other lead connected to a 2-cm diameter copper pad. The copper pad is, in turn, mounted on the end of an insulating rod, such that an individual can press the pad against a single tile without being exposed to the circuit. Current is then run through the circuit and the voltage across the shunt is recorded; 10 and 20 A tests are common. In addition to the calibrated resistance, this process clearly identifies any tiles that may be touching adjacent
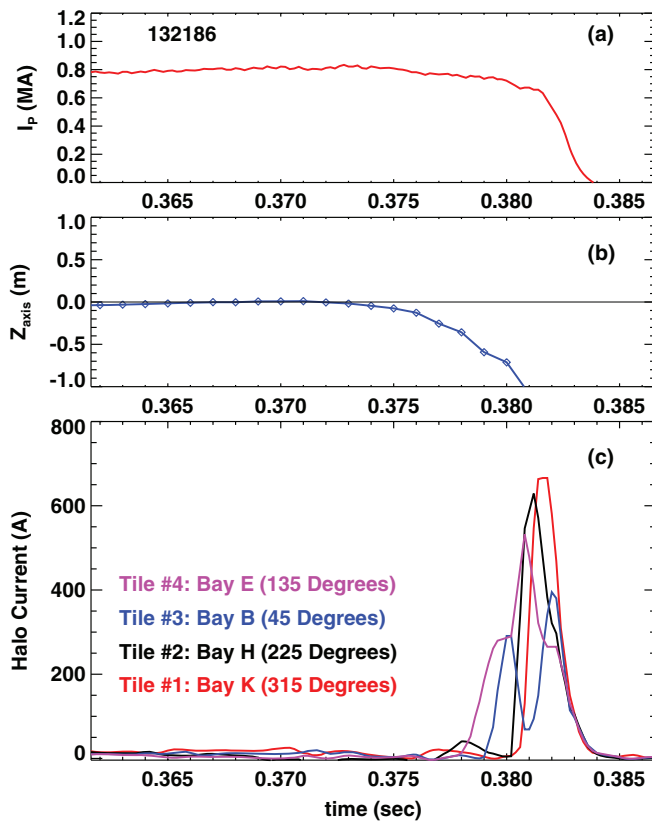
FIG. 8. (Color online) Typical shunt tile signals during a disruption. Shown are (a) the plasma current, (b) the vertical position of the magnetic axis, and (c) the signals from four tiles.
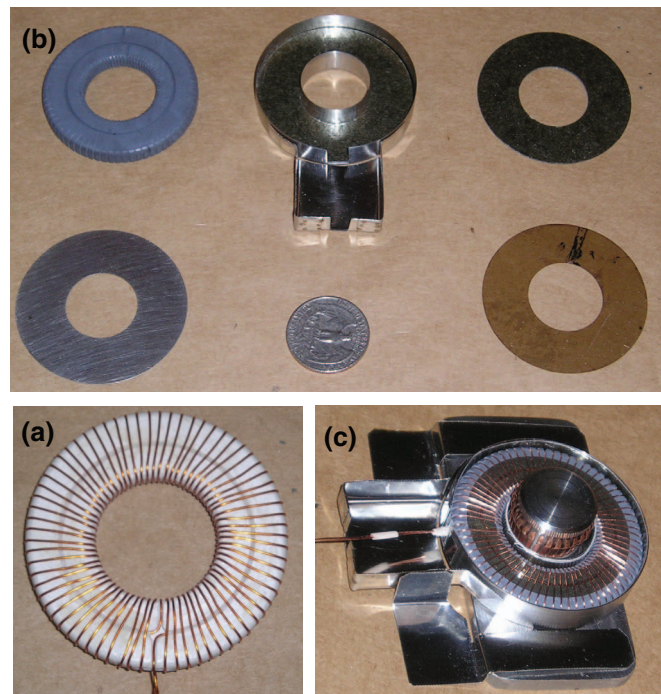

FIG. 9. (Color online) Components of the Rogowski sensor design. Shown are (a) a test mock-up of the Rogowski winding, illustrating the windback trough, (b) the individual components of the assembly, and (c) a nearly complete assembly placed over an LLD center post ground. Note the copper finger-stock on the ground post used to ensure a good electrical connection of the post to the LLD tray. Also, a mica spacer is inserted in (c) between the Rogowksi windings and the loop-back, in order to prevent contact between the windings. In (a) there is a thin layer of FortaFix high-temperature cement covering the loop-back.

tiles, as the sensor voltage will be anomalously low in this case.

Example time-traces from this diagnostic during a disruption are shown in Fig. 8. The top frame shows the plasma current, with the rapid drop at ~0.382 indicating the final disruption; the vertical position of the plasma centroid is shown in frame (b), indicating the downward motion associated with a VDE. The signals from four shunt tiles are indicated in frame (c), showing the expected large spike when the plasma impacts the divertor floor and disrupts.

V. MEASUREMENTS WITH SMALL ROGOWSKI COILS ON THE LIQUID LITHIUM DIVERTOR TRAYS

The thermal and mechanical properties of the LLD trays provide a challenging situation for the halo current measurement. As noted in Sec. I, each tray of the liquid lithium divertor is grounded at a single location via a 1.9-cm diameter post. The space available under these trays is limited, and only 0.95 cm between the top of the copper slats of the divertor floor and the bottom of the LLD tray was provided for the Rogowski sensor. The high operating temperatures of LLD mandate that the sensor be capable of surviving operation at 400 °C (see Fig. 9).

The design resulting from this consideration is shown in Fig. 9. The Rogowski coil is wound on a mandrel formed from high durability boron nitride ZSBN.[28] A uniformly spaced set of sixty-eight 0.6 mm diameter holes were drilled in a circular pattern with diameter 4.78 cm, and then in a concentric circular pattern with radius 2.23 cm, in a 0.64-cm-thick sheet of this material. The sheet was then machined into a small rectangular cross-section torus, with inner and outer diameters equal to the 4.78 and 2.23 cm, respectively. This results in 1/2 of the previously machined small circles being left intact, as winding grooves to hold the conductors of the Rogowski winding. A ~0.2 × 0.2 cm (wide by deep) trough is then machined in the top of the mandrel, for the Rogowski coil wind-back. The cross-sectional area of the final winding is 1.25 cm × 0.64 cm, for a total area of 7.9×10^{-5} m^2.

The winding itself is made from 24 AWG bare copper wire. This conductor is hand wound on the mandrel, ensuring that sufficient separation is maintained between the windings. The two copper leads that come off the sensor are then tungsten inert gas (TIF) welded to stainless-jacketed copper twisted pair wires. Note that use of bare copper wire is common in NSTX magnetic sensors; precision winding, often followed by mechanical stabilization of the winding geometry with high-temperature cement,[29] is a common practice.

In order to protect the Rogowski assembly from the mechanical damage during installation and use, we have placed it in a stainless steel toroidal canister. The bottom, the inner side, and the outer side of the canister are all machined from a single piece of 316-alloy stainless steel to have 0.25 mm wall thickness. A circular cap of the same thickness was also prepared and was spot welded to the can as part of the final
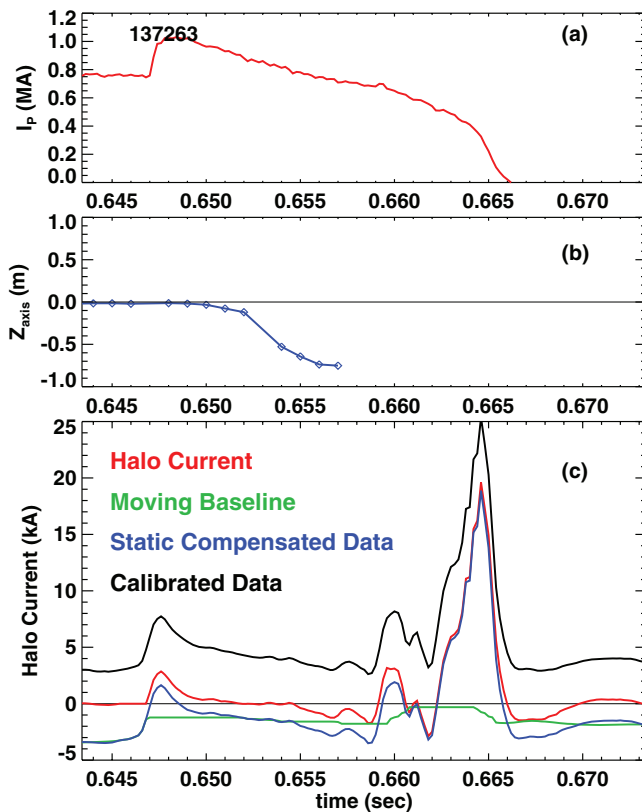
FIG. 10. (Color online) Example data from an LLD grounding post Rogowski coils. Shown are (a) the plasma current, (b) the magnetic axis vertical position, and (c) the signal from the Rogowski sensor (see text for further explanation).

assembly step. The inner and outer walls of the can, as well as the top and bottom, are insulated from the copper turns of the sensors with thin mica sheets and washers.

The sensitivity of the Rogowski coil is given by the quantity $\mu_0 An$, where A is the area of the cross-section and n is the number of turns per unit length. Using 68 turns and a 3.5 cm diameter of the winding for computing the circumference, the inferred sensitivity is 6.13×10^{-8} (V/A)/s. Laboratory tests indicate that the sensitivity is slightly greater, in the vicinity of 6.4×10^{-8} (V/A)/s. When coupled to an integrator with 1 ms time constant, the inferred calibration of the system leads to

$$V_{\text{digitizer}} = \frac{1}{RC} \int \mu_0 AN \frac{dI_{LLD}}{dt} dt = (64 \, \text{mV/kA}) \, I_{LLD},$$

where I_{LLD} is the current flowing into the tray.

Although the ideal Rogowski coil is sensitive to only currents than link the coil, the actual Rogowski sensors are sensitive to other currents in the system (due to non-ideal winding effects), including the plasma current and vessel eddy currents. We used the same median filtering technique as described in Sec. III and shown in Fig. 10(c). The calibrated signal, shown in black, is simply the raw digitizer voltage multiplied by the above calibration factor; there is a large baseline offset. The blue trace shows the static compensated version of the signal (where direct pickup from the coils has been removed). The median filtered of this static compensated signal (green) is then subtracted, yielding the halo current sig-

nal in red. In this case, approximately 20 kA of current flows into the single LLD tray.

[1] J. Wesson, *Tokamaks* (Clarendon, Oxford, England, 1997).
[2] ITER Physics Basis, Nucl. Fusion **39**, 2137 (1999).
[3] T. C. Hender, J. C. Wesley, J. Bialek, A. Bondeson, A. H. Boozer, R. J. Buttery, A. Garofalo, T. P. Goodman, R. S. Granetz, Y. Gribov, O. Gruber, M. Gryaznevich, G. Giruzzi, S. Gunter, N. Hayashi, P. Helander, C. C. Hegna, D. F. Howell, D. A. Humphreys, G. T. A Huysmans, A. W. Hyatt, A. Iasyama, S. C. Jardin, Y. Kawano, A. Kellman, C. Kessel, H. R. Koslowski, R. J. La Haye, E. Lazzaro, Y. Q. Liu, V. Lukash, J. Manickam, S. Medvedev, V. Mertens, S. V. Mirnov, Y. Nakamura, G. Navratil, M. Okabayashi, T. Ozeki, R. Paccagnella, G. Pautsso, F. Porcelli, V. D. Pustovitov, V. Riccardo, M. Sato, O. Sauter, M. J. Schaffer, M. Shimada, P. Sonato, E. J. Strait, M. Sugihara, M. Takechi, A. D. Turnbull, E. Westerhof, D. G. Whyte, R. Yoshino, H. Zohm, and the ITPA MHD, Disruption and Magnetic Control Topical Group, Nucl. Fusion **47**, S128 (2007).
[4] S. P. Gerhardt, J. E. Menard, and the NSTX Team, Nucl. Fusion **49**, 025005 (2009).
[5] Y. Shibata, K. Y. Watanabe, M. Okamoto, N. Ohno, A. Isayama, K. Kurihara, T. Nakano, N. Oyama, Y. Kawano, G. Matsunaga, S. Sakakibara, M. Sugihara, Y. Kamada, and the JT-60 Team, Nucl. Fusion **50**, 025012 (2010).
[6] M. Sugihara, M. Shimada, H. Fujieda, Yu. Gribov, K. Ioki, Y. Kawano, R. Khayrutdinov, V. Lukash, and J. Ohmori, Nucl. Fusion **47**, 337 (2007).
[7] R. J. Hawryluk, D. J. Campbell, G. Janeschitz, P. R. Thomas, R. Albanese, R. Ambrosino, C. Bachmann, L. Baylor, M. Becoulet, I. Benfatto, J. Bialek, A. Boozer, A. Brooks, R. Budny, T. Casper, M. Cavinato, J.-J. Cordier, V. Chuyanov, E. Doyle, T. Evans, G. Federici, M. Fenstermacher, H. Fujieda, K. G'al, A. Garofalo, L. Garzotti, D. Gates, Y. Gribov, P. Heitzenroeder, T. C. Hender, N. Holtkamp, D. Humphreys, I. Hutchinson, K. Ioki, J. Johner, G. Johnson, Y. Kamada, A. Kavin, C. Kessel, R. Khayrutdinov, G. Kramer, A. Kukushkin, K. Lackner, I. Landman, P. Lang, Y. Liang, J. Linke, B. Lipschultz, A. Loarte, G. D. Loesser, C. Lowry, T. Luce, V. Lukash, S. Maruyama, M. Mattei, J. Menard, M. Merola, A. Mineev, N. Mitchell, E. Nardon, R. Nazikian, B. Nelson, C. Neumeyer, J.-K. Park, R. Pearce, R. A. Pitts, A. Polevoi, A. Portone, M. Okabayashi, P. H. Rebut, V. Riccardo, J. Roth, S. Sabbagh, G. Saibene, G. Sannazzaro, M. Schaffer, M. Shimada, A. Sen, A. Sips, C. H. Skinner, P. Snyder, R. Stambaugh, E. Strait, M. Sugihara, E. Tsitrone, J. Urano, M. Valovic, M. Wade, J. Wesley, R. White, D. G. Whyte, S. Wu, M. Wykes, and L. Zakharov, Nucl. Fusion **49**, 065012 (2009).
[8] M. Ono, S. M. Kaye, Y.-K. M. Peng, G. Barnes, W. Blanchard, M. D. Carter, J. Chrzanowski, L. Dudek, R. Ewig, D. Gates, R. E. Hatcher, T. Jarboe, S. C. Jardin, D. Johnson, R. Kaita, M. Kalish, C. E. Kesel, H. W. Kugel, R. Maingi, R. Majeski, J. Manickam, B. McCormack, J. Menard, D. Mueller, B. A. Nelson, B. E. Nelson, C. Neumeyer, G. Oliaro, F. Paoletti, R. Parsells, E. Perry, N. Pomphrey, S. Ramakrishnan, R. Raman, G. Rewoldt, J. Robinson, A. L. Roquemore, P. Ryan, S. Sabbagh, D. Swain, E. J. Synakowski, M. Viola, M. Williams, J. R. Wilson, and the NSTX Team, Nucl. Fusion **40**, 557 (2000).
[9] Y. K. M. Peng and D. J. Strickler, Nucl. Fusion **26**, 769 (1986).
[10] I. H. Hutchinson, *Principles of Plasma Diagnostics* (Cambridge University Press, Cambridge, England, 1987).
[11] H. W. Kugel, M. Bell, L. Berzak, A. Brooks, R. Ellis, S. Gerhardt, H. Harjes, R. Kaita, J. Kallman, R. Maingi, R. Majeski, D. Mansfield, J. Menard, R. E. Nygren, V. Soukhanovskii, D. Stotler, P. Wakeland, and L. E. Zakharov, Fusion Eng. Des. **84**, 1125 (2009).
[12] P. Andrew, P. Noll, V. Riccardo, in *Proceedings of the 17th IEEE/NPSS Symposium on Fusion Engineering*, 1997, p. 108.
[13] V. Riccardo, N. Lam, A. Lawler, D. Starkey, Contributors to the EFDA-JET Workprogramme, Fusion Eng. Des. **66–68**, 919 (2003).

[14] V. Riccardo, T. C. Hender, P. J. Lomas, B. Alper, T. Bolzonella, P. de Vries, G. P. Maddison, and the JET EFDA Contributors, Plasma Phys. Control. Fusion **46**, 925 (2004).

[15] P. J. Knight, G. G. Castle, A. W. Morris, A. Caloutsis, and C. G. Gimblett, Nucl. Fusion **40**, 325 (2000).

[16] R. S. Granetz, I. H. Hutchinson, J. Sorci, J. H. Irby, B. LaBombard, and D. Gwinn, Nucl. Fusion **36**, 545 (1996).

[17] T. Edlington, R. Martin, and T. Pinfold, Rev. Sci. Instrum. **72**, 421 (2001).

[18] G. F. Counsell, R. Martin, T. Pinfold, D. Taylor, and the MAST Team, Plasma Phys. Control. Fusion **49**, 435 (2007).

[19] M. J. Schaffer and B. J. Leikund, Nucl. Fusion **31**, 1750 (1991).

[20] E. J. Strait, L. L Lao, J. L. Luxon, and E. E. Reis, Nucl. Fusion **31**, 527 (1991).

[21] G. Pautasso and O. Gruber, Fus. Sci. Technol. **44**, 716 (2003)

[22] G. Pautasso, L. Giannone, O. Gruber, A. Herrmann, M. Maraschek, K. H. Schuhbeck, and the ASDEX Upgrade Team, Nucl. Fusion **51**, 043010 (2011).

[23] Y. Neyatani, R. Yoshino, Y. Nakamura, and S. Sakurai, Nucl. Fusion **39**, 559 (1999).

[24] N. Pomaro, T. Bolzonella, P. Fiorentin, L. Grando, S. Peruzzo, V. Riccardo, and P. Sonato, Rev. Sci. Instrum. **74**, 1567 (2003).

[25] V. Riccardo, G. Arnoux, P. Beaumont, S. Hacquin, J. Hobirk, D. Howell, A. Huber, E. Joffrin, R. Koslowski, N. Lam, H. Leggate, E. Rachlew, G. Sergienko, A. Stephen, T. Todd, M. Zerbini, R. Delogu, L. Grando, D. Marcuzzi, S. Peruzzo, N. Pomaro, P. Sonato, and JET EFDA Contributors, Nucl. Fusion **49**, 055012 (2009).

[26] N. Pomphrey, J. M. Bialek, and W. Park, Nucl. Fusion **38**, 449 (1998).

[27] D. Gates, J. E. Menard, and R. J. Marsala, Rev. Sci. Instrum. **75**, 5090 (2004).

[28] See http://www.bn.saint-gobain.com/Combat-Solid-ZSBN.aspx for the mechanical and thermal properties of this material.

[29] The typical high-temperature cement used in NSTX is Fortafix. See http://www.fortafix.com/.